

# Geophysical Research Letters

## RESEARCH LETTER

10.1029/2018GL077696

### Key Points:

- The occurrence of seismicity correlates with both pore pressure and poroelastic stresses obtained from poroelastic modeling in the Barnett Shale
- Models of seismicity rate and seismic hazard are sensitive to the rate of Coulomb failure stress change
- Decreasing the injection rate does not necessarily reduce earthquake probability immediately

### Supporting Information:

- Supporting Information S1

### Correspondence to:

 G. Zhai,  
 gzhai@asu.edu

### Citation:

 Zhai, G., & Shirzaei, M. (2018). Fluid injection and time-dependent seismic hazard in the Barnett Shale, Texas. *Geophysical Research Letters*, 45, 4743–4753. <https://doi.org/10.1029/2018GL077696>

Received 26 FEB 2018

Accepted 8 MAY 2018

Accepted article online 11 MAY 2018

Published online 22 MAY 2018

## Fluid Injection and Time-Dependent Seismic Hazard in the Barnett Shale, Texas

 Guang Zhai<sup>1</sup>  and Manoochehr Shirzaei<sup>1</sup> 
<sup>1</sup>School of Earth and Space Exploration, Arizona State University, Tempe, AZ, USA

**Abstract** The Barnett Shale in Texas experienced an increase in seismicity since 2008, coinciding with high-volume deep fluid injection. Despite the spatial proximity, the lack of a first-order correlation between seismic records and the total volume of injected fluid requires more comprehensive geomechanical analysis, which accounts for local hydrogeology. Using time-varying injections at 96 wells and employing a coupled linear poroelastic model, we simulate the spatiotemporal evolution of pore pressure and poroelastic stresses during 2007–2015. The overall contribution of poroelastic stresses to Coulomb failure stress change is ~10% of that of pore pressure; however, both can explain the spatiotemporal distribution of earthquakes. We use a seismicity rate model to calculate earthquake magnitude exceedance probability due to stress changes. The obtained time-dependent seismic hazard is heterogeneous in space and time. Decreasing injection rates does not necessarily reduce probabilities immediately.

**Plain Language Summary** It is believed by scientific communities that disposing of wastewater into deep rock formations may induce earthquakes. However, it has been debated how and when injection operations affect the seismic hazard in a region. Here we investigate how crustal stress changes as fluid seeps into rocks using computer simulations and then implement numerical models linking the evolution of stress to the elevated seismicity on nearby faults. A combination of these computer models with the rule of statistics enables us to constrain temporally variable seismic hazard in a region. Considering Barnett Shale, Texas, a site of intense injection operation between 2007 and 2015, we show that elevated seismic hazard is highly variable in time and space as a result of widespread high-volume, time-varying fluid injection. In contrast to some opinions, decreasing injection volume does not necessarily reduce earthquake probability. Our model and results advance the understanding of hazards associated with induced seismicity in Texas and elsewhere. It can also benefit the communities working on earthquake hazard forecasting.

## 1. Introduction

A variety of human activities, such as water impoundment, underground mining, geological carbon sequestration, hydraulic stimulation of enhanced geothermal system, and fluid injection/extraction associated with oil and gas exploitation, can induce earthquakes (Ellsworth, 2013; Grigoli et al., 2017; Rubinstein & Mahani, 2015). The recent increase of seismicity in the central and eastern United States is suggested to be induced by deep injection of coproduced brine into the subsurface (Ellsworth, 2013). Most of the increased seismic events are found in the proximity of injection wells preceded by high-volume injections (e.g., Frohlich, 2012; Horton, 2012; Keranen et al., 2013; Kim, 2013; Rubinstein et al., 2014). The process of inducing seismicity through injection is well known since the Denver earthquakes triggered at the Rocky Mountain Arsenal (Healy et al., 1968) and the experiments in Rangely earthquake control (Raleigh et al., 1976). However, distinguishing them from natural earthquakes is not straightforward due to poor constraints on local hydrogeology, the background stress field, and the initial pore pressure (Ellsworth, 2013; Grigoli et al., 2017), which can be resolved using structural geology analysis (Magnani et al., 2017).

There are numerous mechanisms impacting the process of injection-induced seismicity, including direct increase of pore pressure reducing effective normal stress through fluid diffusion (Healy et al., 1968; Hubbert & Rubey, 1959), stress perturbation in the medium due to poroelastic stress changes (Barbour et al., 2017; Deng et al., 2016; Segall & Lu, 2015), interaction with induced seismic (Sumy et al., 2014) or aseismic (Guglielmi et al., 2015) slips, thermoelastic response caused by temperature difference of injected fluid and host rocks (Majer et al., 2007), modifying velocity-strengthening frictional properties into velocity-neutral due to increased pore pressure (Scuderi & Collettini, 2016), and reducing rock frictional strength due to geochemical alteration of fracture surfaces (Majer et al., 2007). Most studies addressing the correlation between

injection and nearby seismicity either are qualitative (Ake et al., 2005; Frohlich, 2012) or quantify pore pressure using uncoupled groundwater flow equations (Hornbach et al., 2015; Keranen et al., 2014). Recent studies consider coupling between pore pressure and matrix deformation to investigate the relationship between injection and earthquakes (Deng et al., 2016; Fan et al., 2016; Segall & Lu, 2015; Shirzaei et al., 2016). This relationship is a function of injection rate, local hydrogeology, initial pore pressure and background stress state, fault orientation and permeability, and frictional properties (Chang & Segall, 2016; Fan et al., 2016). Moreover, a delay of months to years is often observed between injection and seismicity, which stems from a low initial pore pressure (Keranen et al., 2013), low rate of fluid diffusion (Keranen et al., 2014), transient fluid flow (Norbeck & Horne, 2016), unsuitable fault orientation, and low background stress. Also, varying injection rates can result in transient and possibly large changes in poroelastic stress and pore pressure rate (Barbour et al., 2017; Segall & Lu, 2015).

The seismic hazard associated with fluid injection is estimated using a reconstructed Gutenberg-Richter law adapted for induced events (Shapiro et al., 2013). This law predicts a probability decrease for large earthquakes immediately after an injection rate decline (Langenbruch & Zoback, 2016), which is in contrast with the not uncommon observation of large earthquakes occurring after injection shut-in (Horton, 2012; Kim, 2013). This is likely because the reconstructed Gutenberg-Richter law is obtained assuming nondecreasing injection rates and is applicable for earthquake magnitudes less than 2.0 (Shapiro, 2015), ignoring time-dependent fluid diffusion and mechanisms of earthquake nucleation. Thus, a comprehensive analysis requires incorporating the rate-and-state friction law into geomechanical modeling (Dieterich et al., 2015; McClure & Horne, 2011; Segall & Lu, 2015). In this approach, the seismicity rate is expressed as a function of space and time, hydrogeological properties, fault geometries, and injection rates. Furthermore, the seismicity rate model acts as an input for the calculation of spatiotemporal earthquake probability, which is important for seismic hazard forecasting.

The Barnett Shale in Texas experienced a dramatic increase in seismicity since 2008, when large-volume coproduced waste fluid was injected into the subsurface. Three major earthquake sequences (Dallas-Fort Worth [DFW] Airport earthquakes, Cleburne earthquakes, and Azle earthquakes) occurred in this area suggesting a causal link between injection and increased seismicity (Frohlich et al., 2011; Hornbach et al., 2015; Justinic et al., 2013). We apply a coupled poroelastic model to simulate the spatiotemporal evolution of pore pressure and poroelastic stresses at the basin-wide scale considering high-volume time-varying injections. The model results combined with geomechanical analysis and seismicity rate theory are used for the evaluation of potential fault activation and estimation of time-dependent seismic hazard.

## 2. Seismic and Injection Data Sets

The seismic data are obtained from the Advanced National Seismic System composite earthquake catalog (ComCat), which contains 203  $M \geq 2.0$  earthquakes from 2008 to 2015 (Figure 1 and Table S3). It is notable that only three earthquakes are recorded in the study area during 1990–2007. Most of the earthquakes are located 5 km deep in the Precambrian crystalline basement overlaid by the Ellenburger formation. In addition, we compile 67 earthquakes located by Frohlich (2012) from 2009 through 2011 (Table S4). Many of these events are absent from ComCat owing to the recording from a local monitoring network used by Frohlich (2012). These events have also a fixed 5 km depths. Cumulative numbers of earthquakes for both ComCat and Frohlich catalogues are shown in Figure S13.

Injection data are provided by Texas Railroad Commission for 96 injection wells within the Barnett Shale for the period 2007–2015, given injection shut-in in December 2015 (Figure 1 and Table S2). The annual total injection volume increases from  $\sim 1.8 \times 10^7$  m<sup>3</sup>/year to  $\sim 3.6 \times 10^7$  m<sup>3</sup>/year during 2007–2011 and then decreases to  $\sim 1.7 \times 10^7$  m<sup>3</sup>/year in 2015 (Figure S1). The injection rate for individual wells has strong temporal variability (Figures 1b and 1c). Most wells inject into the Ellenburger formation, except a few that dispose into shallower zones (Table S2). Each well has an upper limit on the daily injection volume based on the well's individual permit. The maximum upper limit is 35,000 BBLs/day ( $\sim 5565$  m<sup>3</sup>/day; Table S2). Although these wells are injecting into an area adjacent to seismic faults (Figure 1), the overall correlation between the total volume or rate of injected fluid and seismicity rate is poor (Figure S1). This suggests a higher-order relationship between injection and seismicity, enhanced by heterogeneous background stress and local hydrogeology of the relatively large study area.

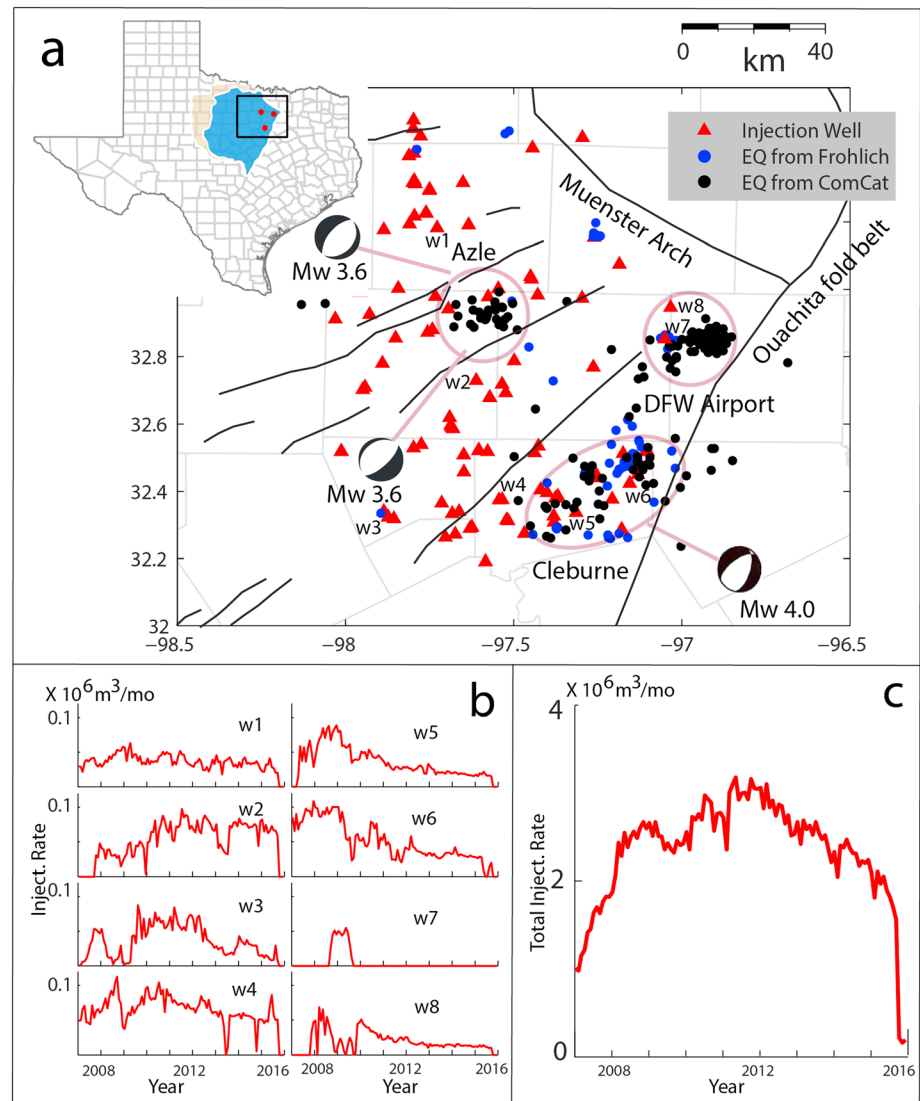


**Figure 1.** The Barnett Shale injection and seismic data for the period 2007–2015. (a) Spatial distribution of 96 injection wells (filled triangles) and earthquakes including earthquakes compiled by Frohlich (2012) in blue filled circles and that from ComCat in black filled circles. Major regional subsurface faults (black lines) and earthquake focal mechanisms are provided by from Hornbach et al. (2015) and U.S. Geological Survey National Earthquake Information Center. The inset shows the study area, and three red dots are center locations of three earthquake sequences at DFW airport, Cleburne, and Azle. Two shaded areas within inset are the Fort Worth basin (grey) and Barnett Shale (blue). (b) Examples of monthly injection rate time series for eight selected wells, whose locations are shown in panel (a). (c) Time series of total injection rate aggregated over all 96 wells.

### 3. Method

We employ a coupled poroelastic model to calculate the spatial and temporal evolution of poroelastic stresses and pore pressure due to fluid injections in the Barnett Shale. Note that the pore pressure estimate through poroelastic modeling is different from wellhead pressure. The wellhead pressure is the pressure at which fluid is injected into the formation matrix, while the term “pore pressure” refers to the change in formation pressure due to the process of fluid diffusion. The governing equations relating the deformation field  $\mathbf{u}$  and pore pressure  $p$ , both of which are a function of location  $\mathbf{x}$  and time  $t$ , are given (Cheng, 2016; Wang & Kümpel, 2003)

$$G\nabla \cdot \nabla \mathbf{u} + \frac{G}{1-2\nu} \nabla(\nabla \cdot \mathbf{u}) - \alpha \nabla p = \mathbf{f}(\mathbf{x}, t) \quad (1)$$

$$\frac{1}{Q} \frac{\partial p}{\partial t} + \alpha \frac{\partial(\nabla \cdot \mathbf{u})}{\partial t} - \nabla \cdot (\chi \nabla p) = q(\mathbf{x}, t) \quad (2)$$

where  $\nabla$  is the gradient operator and  $\nabla \cdot$  is the divergence operator,  $G$  is the shear modulus,  $\nu$  is the drained Poisson ratio,  $\alpha$  is the Biot effective stress coefficient,  $Q$  is the Biot modulus,  $\chi$  is the mobility coefficient defined by the ratio of intrinsic permeability and dynamic fluid viscosity,  $\mathbf{f}$  is the body force per unit bulk volume acting on solid medium, and  $q$  is the volumetric fluid injection rate per unit bulk volume. To characterize a linear poroelastic medium, five independent parameters are needed, including  $G$ ,  $\nu$ , undrained Poisson ratio  $\nu_u$ , hydraulic diffusivity  $D$ , and Skempton coefficient  $B$ . Parameters  $\alpha$ ,  $\chi$ , and  $Q$  can be uniquely determined using these five parameters (Wang & Kumpel, 2003). Equations (1) and (2) are solved by imposing boundary conditions of zero traction and excess pore pressure at the half-space surface (Fan et al., 2016).

The poroelastic model informed by injection and hydrogeological data provides the spatiotemporal distribution of elastic stress tensor derived from  $\mathbf{u}$ ,  $\Delta \mathbf{S}(\mathbf{x}, t)$  and pore pressure change,  $\Delta p(\mathbf{x}, t)$ . Defining the fault orientations and the coefficient of friction  $\mu$ , we calculate the shear stress  $\Delta \tau_s(\mathbf{x}, t)$  and normal stress  $\Delta \sigma(\mathbf{x}, t)$  (positive for unclamping); thus, the Coulomb failure stress (CFS) change  $\Delta \tau(\mathbf{x}, t)$  is given by

$$\Delta \tau = \Delta \tau_s + \mu(\Delta \sigma + \Delta p) = (\Delta \tau_s + \mu \Delta \sigma) + \mu \Delta p \quad (3)$$

Dieterich (1994) developed a framework describing the evolution of seismicity rate as a function of background seismicity rate and CFS change. A simplified version was given by Segall and Lu (2015) relating the relative seismicity rate  $R(\mathbf{x}, t)$  (rate of seismicity relative to the background seismicity rate) to the Coulomb stressing rate  $\dot{\tau}(\mathbf{x}, t)$ :

$$\frac{dR(\mathbf{x}, t)}{dt} = \frac{R(\mathbf{x}, t) \dot{\tau}_0}{A \bar{\sigma}} \left( \frac{\dot{\tau}(\mathbf{x}, t)}{\dot{\tau}_0} - R(\mathbf{x}, t) \right) \quad (4)$$

where  $\dot{\tau}_0$  is the background stressing rate,  $A$  is a constitutive parameter in the rate-and-state friction law,  $\bar{\sigma}$  is the background effective normal stress, and  $\frac{A \bar{\sigma}}{\dot{\tau}_0}$  is the characteristic relaxation time. Table S1 gives the typical values for  $A$  (Segall & Lu, 2015). We use the value of  $10^{-5}$  MPa/year for background stressing rate  $\dot{\tau}_0$ , which is obtained based on a geodetic study of the strain rate of the Northern American plate (Calais et al., 2006).  $\bar{\sigma}$  is 35 MPa at the bottom of the Ellenburger formation, considering a normal stress gradient of 10 MPa/km along depth for high-dip angle faults.

Assuming an inhomogeneous Poisson process for earthquake occurrence, the probability of at least one event larger than  $M$  in time interval  $[t_1, t_2]$  at location  $\mathbf{x}$  is

$$P_{\geq M}(t_1, t_2, \mathbf{x}) = 1 - \exp[-N_{\geq M}(t_1, t_2, \mathbf{x})] \quad (5)$$

where  $N_{\geq M}(t_1, t_2, \mathbf{x})$  is the expected number of  $\geq M$  earthquakes during  $[t_1, t_2]$  at  $\mathbf{x}$ . From equation (4) and assuming a constant background seismicity rate,  $r_{\geq M}(\mathbf{x})$  at  $\mathbf{x}$ , we obtain

$$N_{\geq M}(t_1, t_2, \mathbf{x}) = \int_{t_1}^{t_2} r_{\geq M}(\mathbf{x}) R(\mathbf{x}, t) dt \quad (6)$$

where  $r_{\geq M}(\mathbf{x}) * R(\mathbf{x}, t)$  defines the earthquake rate after stress perturbation for earthquake magnitude larger than  $M$  at location  $\mathbf{x}$  and time  $t$ .  $r_{\geq M}(\mathbf{x})$  is given using Gutenberg-Richter frequency-magnitude relationship and is scaled with grid size  $s(\mathbf{x})$  at  $\mathbf{x}$ :

$$r_{\geq M}(\mathbf{x}) = \frac{s(\mathbf{x})}{S} k 10^{-bM} \quad (7)$$

where  $k$  is the background earthquake rate of magnitude  $\geq 0$ , describing the productivity level in the whole study region with size  $S$ .  $b$  is the slope of frequency-magnitude relationship, characterizing the earthquake size distribution. Considering the spatial proximity of our study area to Oklahoma, we take the  $b$ -value determined using Oklahoma catalog as a reference (Table S1) (Langenbruch & Zoback, 2016). Also, using the historical earthquakes of  $M > 2.0$  within our study area (Table S3; Frohlich et al., 2016; Gono, 2015), we obtain

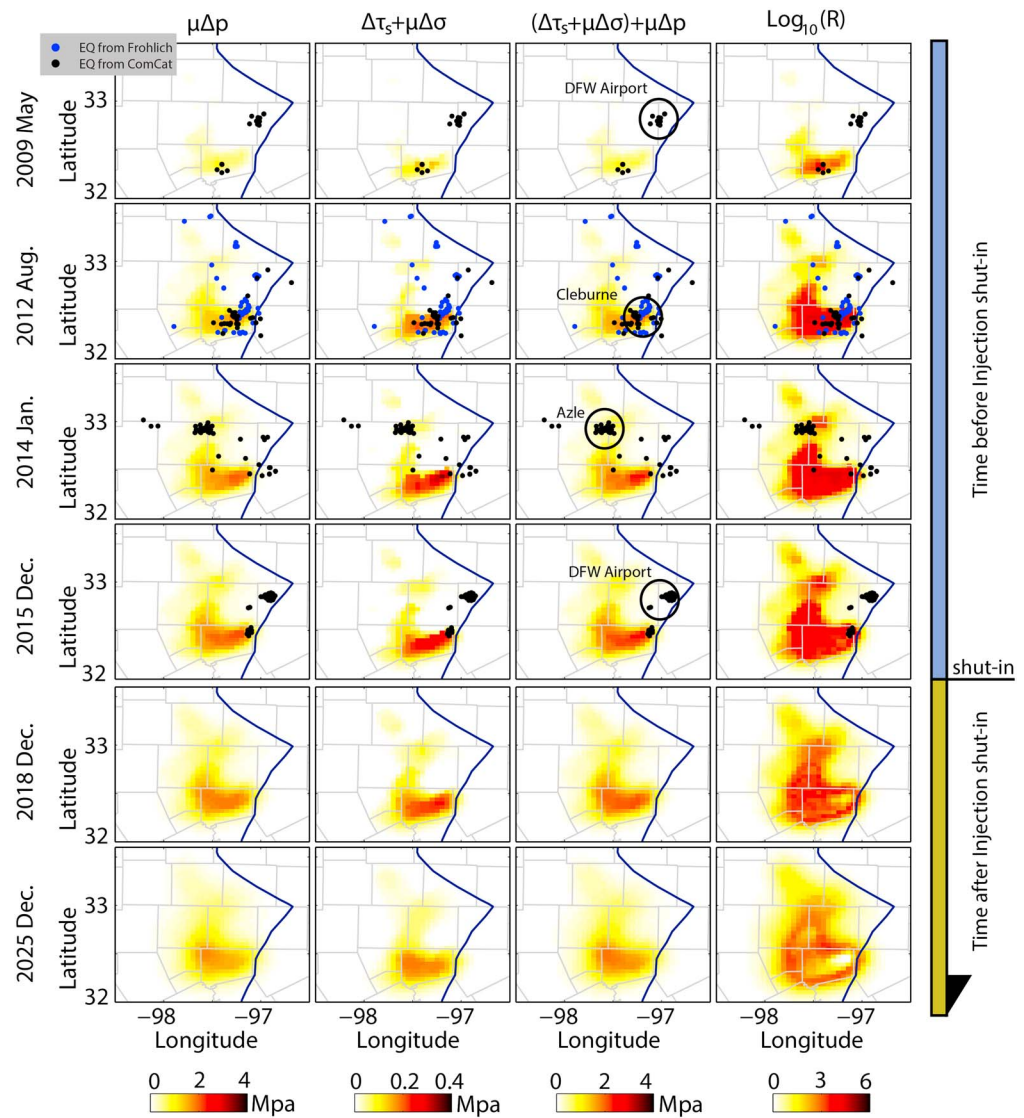


**Figure 2.** Comprises two blocks associated with preinjection and postinjection shut-in on December 2015 and shown are snapshots of the distribution of the modeled cumulative  $\mu\Delta p$ ,  $\Delta\tau_s + \mu\Delta\sigma$ ,  $(\Delta\tau_s + \mu\Delta\sigma) + \mu\Delta p$ , and  $\text{Log}_{10}(R)$  at different times, corresponding with the end of each earthquake sequences, the end of injection operation, and two postinjection epochs. Incremental occurrences of earthquakes from Frohlich (2012) (blue dots) and ComCat (black dots) catalogues are shown before for the preinjection shut-in period. Note the different magnitudes of pore pressure and poroelastic stress. Zones defined for earthquake sequences of DFW Airport, Cleburne, and Azle are marked by black circles. Here  $\mu\Delta p$  is the CFS change due to pore pressure change, scaled by the coefficient of friction;  $\Delta\tau_s + \mu\Delta\sigma$  is the CFS change due to poroelastic stress change;  $(\Delta\tau_s + \mu\Delta\sigma) + \mu\Delta p$  is the total CFS change; and  $\text{Log}_{10}(R)$  is the logarithm of seismicity rate.

that  $k$  value roughly equals to  $10^{1.3}/\text{year}$  (Table S1). We note that the absolute values of seismicity rate and earthquake probability are sensitive to  $k$  and  $b$ , while the relative values are weakly dependent on them.

#### 4. Hydrogeological Background and Model Setup

The availability of hydrogeological data following Hornbach et al. (2016) (Text S1 and Figure S2A) and the depths of injected fluid allow identifying five layers (Figure S2B), characterizing the geomechanical properties of the poroelastic medium (Text S2 and Figure S2C). The main injection layer of the dolomitic Ellenburger formation has a basin-wide depth range of 2,200–3,500 m with an average thickness of 1,300 m in our model (Montgomery et al., 2005; Pollastro et al., 2007; Zhao et al., 2007). The 100-m-thick Barnett Shale formation



acts as a sealing layer atop the Ellenburger formation. The granite basement below 3.5 km is thought to be fractured and hydraulically connected to the Ellenburger formation (Ewing, 1990), hosting most of the observed seismicity. The Ellenburger formation is believed to comprise very low permeability rocks (Gale & Gomez, 2007). The overall stress state in the Barnett Shale is consistent with normal faulting regime (Snee & Zoback, 2016) where high-dip-angle faults are oriented along the northeast (Figure 1). The Cleburne and Azle earthquake sequences involve dip-slip focal mechanism. The focal mechanism of the DFW Airport sequence is not determined but is perceived to be similar to that of the Cleburne and Azle sequences (Frohlich et al., 2011). The optimal receiver fault geometry used for calculating CFS change is summarized in Table S1 (Hornbach et al., 2015; Scales et al., 2017; Snee & Zoback, 2016).

## 5. Result

Using time-varying injected volumes at 96 wells with injection shut-in in December 2015, we simulate the evolution of pore pressure and poroelastic stresses in the study area (Text S3 and Figure S3). Figure 2 shows snapshots of the temporal evolution of pore pressure scaled by the frictional coefficient with a value of 0.6, as well as CFS change due to poroelastic stresses at the bottom of the Ellenburger formation (3.5 km). Note that Figure 2 is divided into two blocks, demonstrating the evolution of parameters prior to and after the assumed injection shut-in in December 2015. Therefore, all model validations are performed only using the block associated with the preshut-in period. We find that the overall effect of pore pressure (maximum of 3.5 MPa) is an order of magnitude larger than that of poroelastic stresses, which is consistent with Chang and Segall (2016).

Visual inspection suggests that the location and timing of the seismicity correspond to zones of increased pore pressure, poroelastic stress, and total CFS change, although the values for DFW Airport sequence appear to be small (Figure 2). The calculated pore pressure following injection shut-in shows a slow decay, consistent with Shirzaei et al. (2016). Also, simulated time-dependent seismicity rates correlate with the location and timing of observed seismicity, but the values for the DFW Airport sequence also appear to be small (Figure 2). Interestingly, although the simulated seismicity rate adjacent to the wells has already dropped following injection shut-in, at further distances, the seismicity rate remains high and then gradually decays.

Given the spatiotemporally variable injections, the patterns and values of CFS change, stressing rate, and time-dependent seismicity rate are different at the locations of seismic swarms (Figures 3a–3c). We define three regions of 20-km radial distance from a swarm center to identify areas affected by the earthquake sequences (Figure 2). For each area, we spatially average the time series of CFS change, stressing rate, and seismicity rate (Figure 3). For DFW Airport, both CFS change and seismicity rate increase with time and they continue to increase beyond injection shut-in. The seismicity rate at Cleburne increases until 2011, then decays to the background level, although the CFS change only gradually decreases after 2015. At Azle, both values increase until 2015, after which the CFS change reaches a persistent high value, while the seismicity rate decreases toward the background value. Figure 3d shows similar parameters as shown in Figures 3a–3c, but now calculation is done for the whole study area. During period 2011–2015, the average CFS change increases and the seismicity rate reaches a steady state. Afterward, the seismicity rate gradually drops, but the average CFS change remains almost constant near its high value. We further test the impact of various  $A$  values and background stressing rates on the estimated seismicity rate for the whole study area (Figure S14). As seen, various combinations result in very different seismicity rate pattern. However, the preferred set of parameters (Table S1) yields an earthquake magnitude exceedance probability (discussed below) that is most consistent with the observed seismicity. Nevertheless, due to the poor quality of seismic data and incompleteness of catalog, performing comprehensive quantitative validation of seismicity rate model is not possible.

The simulated earthquake magnitude exceedance probability is a function of time and location (equation (5)). The local earthquake probability is sensitive to the seismicity rate (or Coulomb stressing rate), as indicated by the relative earthquake probability distribution (Figures 2 and S4). Through spatial integration, we estimate the annual magnitude exceedance probability for different zones (Figure 4) same as those investigated in Figure 3. In the vicinity of the DFW Airport sequence, the exceedance probability continues to increase over time (Figure 4a), as does the seismicity rate (Figure 3a). However, the magnitude of probability increase is less than 6% for magnitude  $\geq 2.0$ . For Cleburne, the annual exceedance probability culminates during years 2011–2014 with a maximum of  $\sim 40\%$  for magnitude  $\geq 4.0$  and then decreases. The probability for magnitude  $\geq 4.0$  is  $\sim 30\%$  in Cleburne in 2015 when the Venus magnitude 4.0 event occurred. In contrast, Azle peaks in 2015,

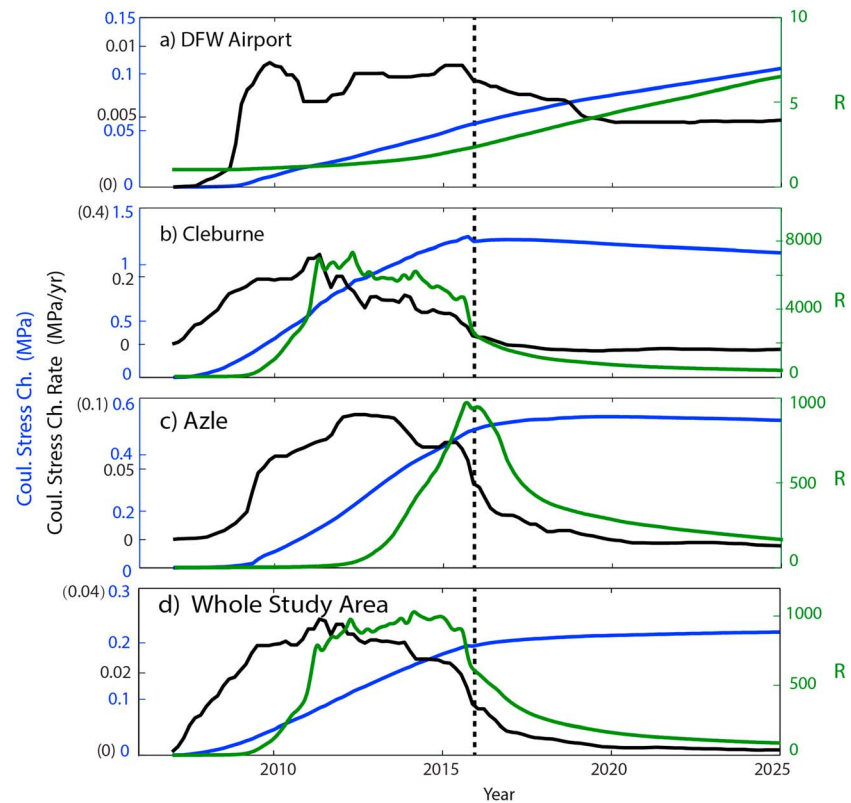


**Figure 3.** Modeled time series of spatially average total CFS change (blue), Coulomb stressing rate (black), and relative seismicity rate (green) for zones of (a) DFW Airport, (b) Cleburne, (c) Azle, and (d) the whole study area. The vertical dashed lines show the timing of injection shut-in. The Coulomb stressing rate is smoothed using six-month moving average window.

followed by a decaying period. During 2015, the exceedance probability for magnitude  $\geq 4.0$  is  $\sim 8\%$ . We also evaluate the magnitude exceedance probability for the whole study area (Figure 4d). Three distinct episodes for the annual probability change are identified including an increasing period from 2007 to 2011, a steady episode of 2011–2015, and a decaying period following 2015. The steady episode has a yearly probability of  $\sim 60\%$  for magnitude  $\geq 4.0$ .

## 6. Discussion and Summary

The linear poroelastic model is characterized by five layers in half space, and each layer is assumed to be homogeneous, isotropic, and porous. However, this is an idealized description of an inherently complex medium. In the Barnett Shale, the Ellenburger formation and underlying basement are fractured (Ewing, 1990), enhancing permeability. The existence of paleokarst may also increase permeability. Using the upper value of  $0.7 \text{ m}^2/\text{s}$  for hydraulic diffusivity (Hornbach et al., 2015), we obtained new poroelastic, seismicity rate, and earthquake probability models (Figures S5–S6). As seen, increasing the hydraulic diffusivity results in pore pressure and seismicity rates with broader spatial distribution, although the maximum magnitudes are reduced (Figures S3 and S5). This leads to the reduction of annual exceedance probability for  $M \geq 4.0$  earthquakes from 60% to 40% for the whole area. It also modifies the temporal pattern of annual earthquake probabilities (Figures 4d and S6). Moreover, well logs and seismic imaging show that subsurface architectures are not perfect layers with equal thicknesses, which can alter fluid diffusion. Investigating such effect on earthquake probability is a subject of future studies. The interaction between permeability and pore pressure may alter the estimated stress changes because permeability is pressure dependent, but this effect likely has a secondary impact on the results compared with other model uncertainties.

Although most earthquakes occur in zones of increased CFS change or predicted high seismicity rates, there are zones subject to elevated CFS change lacking elevated seismicity. This may be attributed to

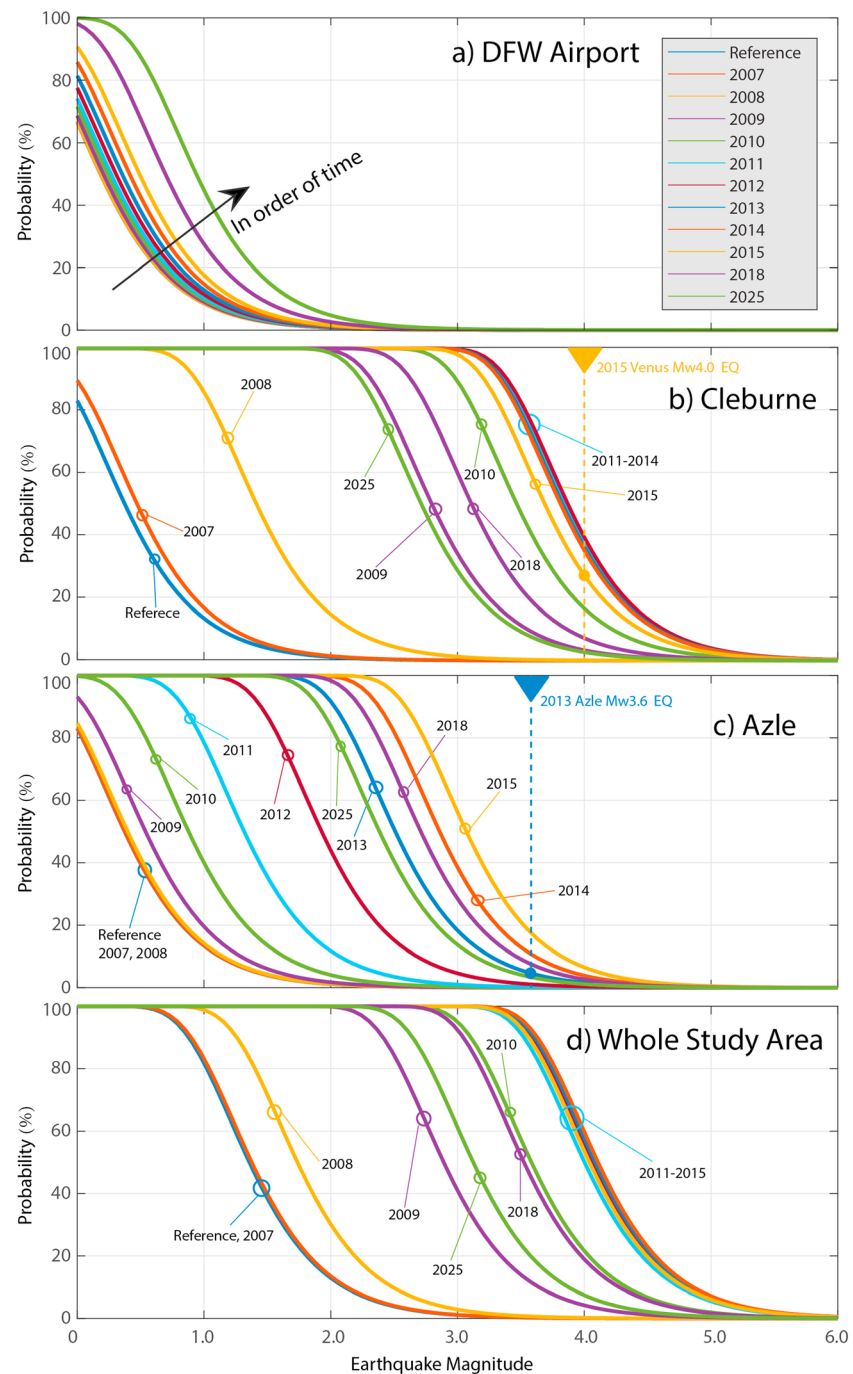


**Figure 4.** Annual earthquake magnitude exceedance probabilities for (a) DFW Airport, (b) Cleburne, (c) Azle, and (d) the whole study area for different years. The vertical dashed lines indicate the largest magnitudes of earthquakes occurred in Cleburne and Azle, color-coded with the associated year.

heterogeneous background tectonic stresses or initial pore pressures, the absence of faults, and/or heterogeneous fault orientations. Due to the low permeability of the injection layer, the prediction of CFS change after injection shut-in exhibits a slowly decaying pattern (Figures 2 and 3). The large postinjection CFS change may expedite earthquake occurrence (e.g., clock advance in the context of the earthquake cycle), which could have a longer-lasting effect on earthquake probability. However, the calculation of this effect requires detailed knowledge of the earthquake cycle for a preexisting fault, which is unavailable.



Also, the seismicity rate model presented here (equation (4)) only predicts rupture nucleation rate and does not account for the effect of interactions between adjacent ruptures (Segall & Lu, 2015). Future works need to be done to overcome this limitation.

Our model depicts an outward propagating seismicity front after injection shut-in following December 2015 (Figures 2 and S3), where fluid continues to propagate and transiently changes the stress state (Segall & Lu, 2015). Following shut-in, the seismicity rate within the zone of high-rate injections (near-field) drops faster than that of outside (far-field). During injection, both pore pressure and poroelastic stresses contribute to the CFS change. After injection shut-in, the pore pressure in the near-field decreases faster; however, due to the process of fluid diffusion, the pore pressure declining rate decreases in the far-field. Also, note that following injection shut-in, poroelastic stresses decrease but their contribution to the total CFS change is too small to make a noticeable impact.

The maps of CFS change indicate that different amounts of stress change are needed to trigger an earthquake sequence at different locations (Figures 3a–3c and S13). For DFW Airport, the earthquake sequence starts almost at the beginning of injection with CFS increase of  $\sim 0.005$  MPa. This indicates either the faults in this area were critically stressed prior to injection, our isotropic poroelastic model is overly simplified, or a combination of both. We also cannot rule out the possibility that the DFW Airport sequence is of natural origin. At Cleburne and Azle, the required CFS change for the first events to occur is 0.35–0.4 MPa. In late 2015 another earthquake sequence occurred near DFW Airport, accompanied by a continuous increase of CFS change (Figures 2 and 3a). The timing of the earthquake sequences shows that they occur once CFS change increases by 0.05 MPa. Examining the spatiotemporal evolution of earthquakes recorded by ComCat, two other earthquake sequences occurred in the Cleburne zone (e.g., Gono, 2015), which are noted as sharp increases in cumulative earthquake count (Figure S13). This suggests a recurring pattern for seismic swarms following CFS change of 0.45–0.5 MPa (Figure 3b). However, the Azle earthquake record is too sparse to allow such an examination.

We obtain regional estimates of time-dependent earthquake probability caused by stress field perturbation due to fluid injection. The results highlight the importance of the stressing rate for earthquake probability change, which can be orders of magnitude above the background probability (Figure S4). The key to probability calculation is predicting the seismicity rate dependent on the injection-induced stress history (Figures 3 and 4). The average CFS change increases linearly from 2011–2015, corresponding with a steady stressing rate (Figure 3d). Accordingly, the annual magnitude exceedance probability almost remains unchanged during the same period (Figure 4d). After 2015, the average CFS change reaches a steady state accompanied by a period of decaying seismicity rate and decreasing annual magnitude exceedance probability (Figures 3d and 4d). This implies that after injection shut-in, the earthquake probability reduces due to a rapid decrease of CFS change. However, during a period of decreasing injection rate from 2011 through 2015 (Figure 1c), the stressing rate and earthquake probability do not decrease immediately. This is because the time-dependent poroelastic process positively contributes to the stressing rate. This is opposite to the direct effect of a declining injection rate on the CFS change. These results demonstrate that the change in injection-induced earthquake probability is highly time-dependent because of the temporally variable nature of the poroelastic process and injection rate.

In addition to fluid injection, brine is possibly produced, especially at Azle, from the Ellenburger formation along with hydraulic fracturing (Hornbach et al., 2015). This volume of extracted fluid may change the pore pressure within the formation, revising the total CFS change. To investigate this effect, we use the data from Hornbach et al. (2015) for 120 production wells at Azle (Figure S7) and evaluate the associated CFS change due to production volume (Text S4 and Figures S8–12). We find the impacts of brine production on stress change and seismicity rate at Azle are negligible. However, the data set of production wells is not complete, and the true impact of fluid extraction can be much larger. This highlights the need for new regulations to require operators to release production data in a timely fashion.

## References

- Ake, J., Mahrer, K., O'Connell, D., & Block, L. (2005). Deep-injection and closely monitored induced seismicity at Paradox Valley, Colorado. *Bulletin of the Seismological Society of America*, 95(2), 664–683. <https://doi.org/10.1785/0120040072>
- Barbour, A. J., Norbeck, J. H., & Rubinstein, J. L. (2017). The effects of varying injection rates in Osage County, Oklahoma, on the 2016 Mw 5.8 Pawnee earthquake. *Seismological Research Letters*. <https://doi.org/10.1785/0220170003>

## Acknowledgments

The authors would like to thank Bill Ellsworth, Paul Segall, and two anonymous reviewers for helpful comments that significantly improved the manuscript. We thank the Texas Railroad Commission for making the injection time series publicly available and Matt Hornbach for providing the production data at Azle. We also appreciate Megan Miller for carefully proofreading the manuscript. Injection well data are downloaded from Railroad Commission of Texas (<http://webapps.rrc.state.tx.us/H10/h10PublicMain.do>), and earthquake catalogues are obtained from ANSS Comprehensive Earthquake Catalog (<https://earthquake.usgs.gov/earthquakes/search/>) and Frohlich (2012). We include the lists of injection wells and seismicity in the supporting information. The research is partly supported by National Science Foundation grant EAR1344424 and National Aeronautics and Space Administration grant NNX17AD98G.

- Calais, E., Han, J. Y., DeMets, C., & Nocquet, J. M. (2006). Deformation of the North American plate interior from a decade of continuous GPS measurements. *Journal of Geophysical Research*, 111, B06402. <https://doi.org/10.1029/2005JB004253>
- Chang, K. W., & Segall, P. (2016). Injection-induced seismicity on basement faults including poroelastic stressing. *Journal of Geophysical Research: Solid Earth*, 121, 2708–2726. <https://doi.org/10.1002/2015JB012561>
- Cheng, A. H.-D. (2016). *Poroelasticity* (Vol. 27). Dordrecht, Netherlands: Springer.
- Deng, K., Liu, Y., & Harrington, R. M. (2016). Poroelastic stress triggering of the December 2013 Crooked Lake, Alberta, induced seismicity sequence. *Geophysical Research Letters*, 43, 8482–8491. <https://doi.org/10.1002/2016GL070421>
- Dieterich, J. H. (1994). A constitutive law for rate of earthquake production and its application to earthquake clustering. *Journal of Geophysical Research*, 99, 2601–2618. <https://doi.org/10.1029/93JB02581>
- Dieterich, J. H., Richards-Dinger, K. B., & Kroll, K. A. (2015). Modeling injection-induced seismicity with the physics-based earthquake simulator RSQSim. *Seismological Research Letters*, 86(4), 1102–1109. <https://doi.org/10.1785/0220150057>
- Ellsworth, W. L. (2013). Injection-Induced Earthquakes. *Science*, 341(6142). <https://doi.org/10.1126/science.1225942>
- Ewing, T. E. (1990). *Tectonic map of Texas*. Bureau of Economic Geology, University of Texas at Austin.
- Fan, Z., Eichhubl, P., & Gale, J. F. (2016). Geomechanical analysis of fluid injection and seismic fault slip for the Mw 4.8 Timpson, Texas, earthquake sequence. *Journal of Geophysical Research: Solid Earth*, 121, 2798–2812. <https://doi.org/10.1002/2016JB012821>
- Frohlich, C. (2012). Two-year survey comparing earthquake activity and injection-well locations in the Barnett Shale, Texas. *Proceedings of the National Academy of Sciences of the United States of America*, 109(35), 13,934–13,938. <https://doi.org/10.1073/pnas.1207728109>
- Frohlich, C., Hayward, C., Stump, B., & Potter, E. (2011). The Dallas-Fort Worth earthquake sequence: October 2008 through May 2009. *Bulletin of the Seismological Society of America*, 101(1), 327–340. <https://doi.org/10.1785/0120100131>
- Frohlich, C., Walter, J. I., DeShon, H., Stump, B., Hayward, C., & Hornbach, M. (2016). A historical review of induced earthquakes in Texas. *Seismological Research Letters*, 87(4), 1022–1038. <https://doi.org/10.1785/0220160016>
- Gale, J. F., & Gomez, L. A. (2007). Late opening-mode fractures in karst-brecciated dolostones of the Lower Ordovician Ellenburger Group, west Texas: Recognition, characterization, and implications for fluid flow. *AAPG Bulletin*, 91(7), 1005–1023. <https://doi.org/10.1306/03130706066>
- Gono, V. (2015). *On shaky ground: Understanding the correlation between induced seismicity and wastewater injection in the Fort Worth basin*. (Master of Science in Engineering Master), The University of Texas at Austin.
- Grigoli, F., Cesca, S., Priolo, E., Rinaldi, A. P., Clinton, J. F., Stabile, T. A., et al. (2017). Current challenges in monitoring, discrimination, and management of induced seismicity related to underground industrial activities: A European perspective. *Reviews of Geophysics*, 55, 310–340. <https://doi.org/10.1002/2016RG000542>
- Guglielmi, Y., Cappa, F., Avouac, J. P., Henry, P., & Ellsworth, D. (2015). Seismicity triggered by fluid injection-induced aseismic slip. *Science*, 348(6240), 1224–1226. <https://doi.org/10.1126/science.aab0476>
- Healy, J. H., Rubey, W. W., Griggs, D. T., & Raleigh, C. B. (1968). The Denver earthquakes. *Science*, 161(3848), 1301–1310. <https://doi.org/10.1126/science.161.3848.1301>
- Hornbach, M. J., DeShon, H. R., Ellsworth, W. L., Stump, B. W., Hayward, C., Frohlich, C., et al. (2015). Causal factors for seismicity near Azle, Texas. *Nature Communications*, 6(6728). <https://doi.org/10.1038/ncomms7728>
- Hornbach, M. J., Jones, M., Scales, M., DeShon, H. R., Magnani, M. B., Frohlich, C., et al. (2016). Ellenburger wastewater injection and seismicity in North Texas. *Physics of the Earth and Planetary Interiors*, 261, 54–68. <https://doi.org/10.1016/j.pepi.2016.06.012>
- Horton, S. (2012). Disposal of Hydrofracturing waste fluid by injection into subsurface aquifers triggers earthquake swarm in Central Arkansas with potential for damaging earthquake. *Seismological Research Letters*, 83(2), 250–260. <https://doi.org/10.1785/gssrl.83.2.250>
- Hubbert, M. K., & Rubey, W. W. (1959). Role of fluid pressure in mechanics of overthrust faulting. *Geological Society of America Bulletin*, 70, 11–166.
- Justinic, A. H., Stump, B., Hayward, C., & Frohlich, C. (2013). Analysis of the Cleburne, Texas, earthquake sequence from June 2009 to June 2010. *Bulletin of the Seismological Society of America*, 103(6), 3083–3093. <https://doi.org/10.1785/0120120336>
- Keranen, K. M., Savage, H. M., Abers, G. A., & Cochran, E. S. (2013). Potentially induced earthquakes in Oklahoma, USA: Links between wastewater injection and the 2011 Mw 5.7 earthquake sequence. *Geology*, 41(6), 699–702. <https://doi.org/10.1130/g34045.1>
- Keranen, K. M., Weingarten, M., Abers, G. A., Bekins, B. A., & Ge, S. (2014). Sharp increase in central Oklahoma seismicity since 2008 induced by massive wastewater injection. *Science*, 345(6195), 448–451. <https://doi.org/10.1126/science.1255802>
- Kim, W.-Y. (2013). Induced seismicity associated with fluid injection into a deep well in Youngstown, Ohio. *Journal of Geophysical Research: Solid Earth*, 118, 3506–3518. <https://doi.org/10.1002/jgrb.50247>
- Langenbruch, C., & Zoback, M. D. (2016). How will induced seismicity in Oklahoma respond to decreased saltwater injection rates? *Science Advances*, 2(11), e1601542. <https://doi.org/10.1126/sciadv.1601542>
- Magnani, M. B., Blanpied, M. L., DeShon, H. R., & Hornbach, M. J. (2017). Discriminating between natural versus induced seismicity from long-term deformation history of intraplate faults. *Science Advances*, 3(11), e1701593. <https://doi.org/10.1126/sciadv.1701593>
- Majer, E. L., Baria, R., Stark, M., Oates, S., Bommer, J., Smith, B., & Asanuma, H. (2007). Induced seismicity associated with enhanced geothermal systems. *Geothermics*, 36(3), 185–222. <https://doi.org/10.1016/j.geothermics.2007.03.003>
- McClure, M. W., & Horne, R. N. (2011). Investigation of injection-induced seismicity using a coupled fluid flow and rate/state friction model. *Geophysics*, 76(6), WC181–WC198. <https://doi.org/10.1190/geo2011-0064.1>
- Montgomery, S. L., Jarvie, D. M., Bowker, K. A., & Pollastro, R. M. (2005). Mississippian Barnett Shale, Fort Worth basin, north-central Texas: Gas-shale play with multi-trillion cubic foot potential. *AAPG Bulletin*, 89(2), 155–175. <https://doi.org/10.1306/09170404042>
- Norbeck, J. H., & Horne, R. N. (2016). Evidence for a transient hydromechanical and frictional faulting response during the 2011 Mw 5.6 Prague, Oklahoma earthquake sequence. *Journal of Geophysical Research: Solid Earth*, 121, 8688–8705. <https://doi.org/10.1002/2016JB013148>
- Pollastro, R. M., Jarvie, D. M., Hill, R. J., & Adams, C. W. (2007). Geologic framework of the Mississippian Barnett Shale, Barnett-Paleozoic total petroleum system, bend arch-Fort Worth Basin, Texas. *AAPG Bulletin*, 91(4), 405–436. <https://doi.org/10.1306/10300606008>
- Raleigh, C. B., Healy, J. H., & Bredehoeft, J. D. (1976). An experiment in earthquake control at Rangely, Colorado. *Science*, 191(4233), 1230–1237. <https://doi.org/10.1126/science.191.4233.1230>
- Rubinstein, J. L., Ellsworth, W. L., McGarr, A., & Benz, H. M. (2014). The 2001-present induced earthquake sequence in the Raton Basin of Northern New Mexico and Southern Colorado. *Bulletin of the Seismological Society of America*, 104(5), 2162–2181. <https://doi.org/10.1785/0120140009>
- Rubinstein, J. L., & Mahani, A. B. (2015). Myths and facts on wastewater injection, hydraulic fracturing, enhanced oil recovery, and induced seismicity. *Seismological Research Letters*, 86(4), 1060–1067. <https://doi.org/10.1785/0220150067>

- Scales, M. M., DeShon, H. R., Magnani, M. B., Walter, J. I., Quinones, L., Pratt, T. L., & Hornbach, M. J. (2017). A decade of induced slip on the causative fault of the 2015 Mw 4.0 Venus earthquake, Northeast Johnson County, Texas. *Journal of Geophysical Research: Solid Earth*, 122, 7879–7894. <https://doi.org/10.1002/2017JB014460>
- Scuderi, M. M., & Collettini, C. (2016). The role of fluid pressure in induced vs. triggered seismicity: Insights from rock deformation experiments on carbonates. *Scientific Reports*, 6, 24852.
- Segall, P., & Lu, S. (2015). Injection-induced seismicity: Poroelastic and earthquake nucleation effects. *Journal of Geophysical Research: Solid Earth*, 120, 5082–5103. <https://doi.org/10.1002/2015JB012060>
- Shapiro, S. A. (2015). *Fluid-induced seismicity*. Cambridge University Press. <https://doi.org/10.1017/CBO9781139051132>
- Shapiro, S. A., Kruger, O. S., & Dinske, C. (2013). Probability of inducing given-magnitude earthquakes by perturbing finite volumes of rocks. *Journal of Geophysical Research: Solid Earth*, 118, 3557–3575. <https://doi.org/10.1002/jgrb.50264>
- Shirzaei, M., Ellsworth, W. L., Tiampo, K. F., González, P. J., & Manga, M. (2016). Surface uplift and time-dependent seismic hazard due to fluid injection in eastern Texas. *Science*, 353(6306), 1416–1419. <https://doi.org/10.1126/science.aag0262>
- Snee, J. E. L., & Zoback, M. D. (2016). State of stress in Texas: Implications for induced seismicity. *Geophysical Research Letters*, 43, 10,208–10,214. <https://doi.org/10.1002/2016GL070974>
- Sumy, D. F., Cochran, E. S., Keranen, K. M., Wei, M., & Abers, G. A. (2014). Observations of static Coulomb stress triggering of the November 2011 M5.7 Oklahoma earthquake sequence. *Journal of Geophysical Research: Solid Earth*, 119, 1904–1923. <https://doi.org/10.1002/2013JB010612>
- Wang, R., & Kumpel, H.-J. (2003). Poroelasticity: Efficient modelling of strongly coupled, slow deformation processes in a multilayered half-space. *Geophysics*, 68(2), 705–717. <https://doi.org/10.1190/1.1567241>
- Wang, R. J., & Kumpel, H. J. (2003). Poroelasticity: Efficient modeling of strongly coupled, slow deformation processes in a multilayered half-space. *Geophysics*, 68(2), 705–717. <https://doi.org/10.1190/1.1567241>
- Zhao, H., Givens, N. B., & Curtis, B. (2007). Thermal maturity of the Barnett Shale determined from well-log analysis. *AAPG Bulletin*, 91(4), 535–549. <https://doi.org/10.1306/10270606060>